Article

Mesoscopic Klein-Schwinger effect in graphene

In the format provided by the
authors and unedited

Contents

I. SCHWINGER EFFECT IN VARIOUS DIMENSIONS

Quantum electrodynamics predicts a pair creation rate, per unit volume, area or length depending on dimensionality, as given by [1], with $E_S = \frac{m^2 c^3}{e\hbar}$ the Schwinger field,

$$w_{3d} = \frac{(eE)^2}{4\pi^3 c\hbar^2} \sum_{n\geq 1} \frac{e^{-n\pi\frac{E_S}{E}}}{n^2} \quad , \quad w_{2d} = \frac{eE}{2\pi^2\hbar}\sqrt{\frac{eE}{c\hbar}} \sum_{n\geq 1} \frac{e^{-n\pi\frac{E_S}{E}}}{n^{3/2}} \quad , \quad w_{1d} = \frac{eE}{\pi\hbar} \sum_{n\geq 1} \frac{e^{-n\pi\frac{E_S}{E}}}{n} \quad . \tag{1}$$

When adapted to condensed matter, speed of light c is replaced by Fermi velocity v_F and the rest energy is substituted with the gap Δ_S. The pair partners being dissociated in the strong electric field, one can thus write a mesoscopic pair current, with a mesoscopic Schwinger field $E_S = \frac{\Delta_S^2}{e\hbar v_F}$ and voltage $V_S = \frac{\Lambda\Delta_S^2}{e\hbar v_F}$, as

$$J_{3d} = \frac{e^2 E^2 \Lambda}{2\pi^3 v_F \hbar^2} \sum_{n\geq 1} \frac{e^{-n\pi\frac{E_S}{E}}}{n^2} \quad , \quad J_{2d} = \frac{2g_s g_v e^2}{\pi h}\sqrt{\frac{e\Lambda^2}{\hbar v_F}} E^{3/2} \sum_{n\geq 1} \frac{e^{-n\pi\frac{E_S}{E}}}{n^{3/2}} \tag{2}$$

$$I_{1d} = \frac{4g_s g_v e^2}{h} V_{ds} \sum_{n\geq 1} \frac{e^{-n\pi\frac{V_S}{V_{ds}}}}{n} \quad . \tag{3}$$

Not specific to Schwinger effect, the $J_{3d} \propto E^2 e^{-\frac{Cte}{E}}$ is reminiscent of field emission according to the Fowler-Nordheim mechanism, which is a non-relativistic variant, corresponding to quantum tunneling across a triangular barrier [2,3], with

$$J_{FN} = \frac{e^3 m_0 E^2}{16\pi^2 m^* \hbar \phi} e^{-\pi\frac{E_{FN}}{E}} \quad , \quad E_{FN} = \frac{4\sqrt{2m^*\phi^3}}{3\pi e\hbar} \sim \frac{4\sqrt{2}}{3\pi}\frac{\phi^2}{e\hbar v_F} \quad , \tag{4}$$

where m_0 and m^* are the bare and effective electron masses, ϕ is the barrier height. It differs from Eq.(2) in the non-universal character of the pre-factor and critical field.

Mesoscopic Schwinger effect has been considered to describe non-linear transport in gapless neutral 2d-graphene [4–8], with :

$$E_S = 0 \qquad J_{2d} = 2.612 \frac{2g_s g_v e^2}{\pi h}\sqrt{\frac{e\Lambda^2}{\hbar v_F}} E^{3/2} \quad , \tag{5}$$

where Λ is the length of the charge neutrality region, and $g_s = g_v = 2$ are the spin and valley degeneracy of graphene. The non-linear Schwinger-pair contribution exceeds the single particle tunneling conductivity $\sigma_{2d} = \frac{g_s g_v e^2}{\pi h}$ [9,10] above a bias voltage $V_{2d} \sim \hbar v_F/e\Lambda \sim 1\text{mV}$ (for $\Lambda = 1\mu\text{m}$).
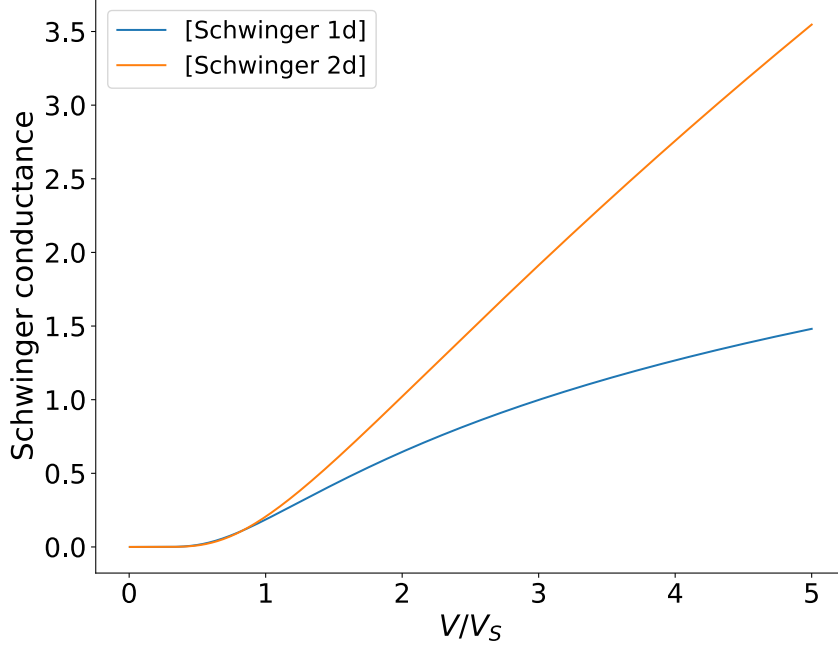
FIG. SI-1: Representation of the functional forms (terms in brackets) of equations (6) and (7) for 1d and 2d massive Schwinger effect. The two forms have the same threshold and low-bias development but differ at large bias. The 2d conductance is not universal and depends on the ratio of the sample width W to the Compton length Λ_C which is typically a large number. It is larger but also linear over a wider bias range than the 1d-Schwinger conductance.

The 2d massive Schwinger effect differs from the 1d massive Schwinger effect studied in the main text. The 1d and 2d conductance read :

$$G_{1d} = 4 \quad \left(\frac{g_s g_v e^2}{h}\right) \times \left[\pi\sqrt{\frac{V}{V_S}}\frac{1}{e^{\pi V_S/V}-1} + \ln\left(\frac{1}{1-e^{-\pi V_S/V}}\right)\right] \tag{6}$$

$$G_{2d} = \frac{2W}{\pi\Lambda_C}\left(\frac{g_s g_v e^2}{h}\right) \times \left[\frac{3}{2}\sqrt{\frac{V}{V_S}}\sum_{n\geq 1}\frac{e^{-n\pi V_S/V}}{n^{3/2}} + \pi\sqrt{\frac{V_S}{V}}\sum_{n\geq 1}\frac{e^{-n\pi V_S/V}}{n^{1/2}}\right] \quad , \tag{7}$$

where W is the sample width and $\Lambda_C = \sqrt{\frac{v_F \hbar}{eE_S}} \lesssim 10\mathrm{nm}$ the Compton length. Compared to the 1d Schwinger conductance, the 2d-conductance prefactor is not universal and much larger by a factor $W/\Lambda_C(V_g) \sim 1000$. Evidence of the universal character of the measured conductance in the ballistic transistors is given in Figure SI-7 and Figure 3-b from the main text, that all show the same universal zero-bias affine extrapolate $G_0 = 0.18 \pm 0.02$ mS despite contrasted values of W and E_S. Apart from the prefactor, the two formulae also show different behavior with respect to bias voltage, as shown in Figure SI-1. The sublinear

dependence of the 1d-conductance of Eq.(6) is clearly seen in Fig. SI-7d) and e), and in Figure 3-d from the main text.
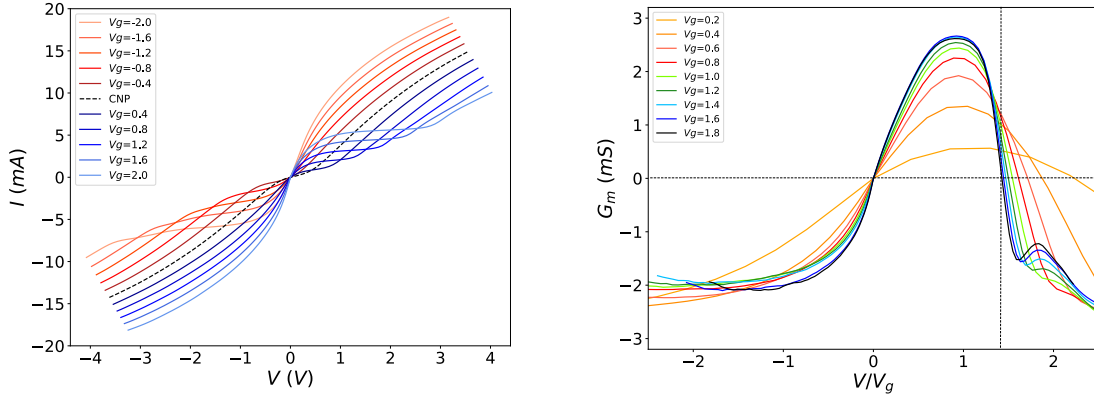

FIG. SI-2: Overview of ballistic pinch-off in hBN-encapsulated graphene transistor GrS1, of dimensions $L \times W \times t_{hBN} = 13 \times 17 \times 0.025$ μm, mobility $\mu = 6.3$ m^{2}V^{-1}s^{-1}, and contact resistance $R_c = 80$ Ω. Left: full bipolar representation. Pinch-off free transport is observed in the drain carrier accumulation regime for $\text{Sign}(V \times V_g) < 0$. It shows standard intra-band velocity saturation by optical phonons (OP), followed by the Zener regime. Pinch-off is observed under drain depletion, for a channel voltage $V = V_{bias} - R_c I \sim V_g$, with broad ($V \sim 0.3$–$1.5V_g$) current plateaus. Pinch-off current is depleted by a factor two below the drain-accumulation counterpart, falling below the massless charge neutrality Zener level (CNP, black dotted line). Pinch-off plateaus terminate as an instability toward the ohmic Zener regime, which is rejected here above $V_Z \gtrsim 1.5V_g$ by Pauli blocking. Right: DC transconductance scaling as function of V/V_g, concentrating on positive V_g values. It underlines the asymmetry between positive and negative V regimes, with a negative transconductance for negative V, illustrating the increase of current with increasing doping. For positive V, the transconductance turns strongly negative, highlighting the depletion of the pinch-off current below the zero-doping CNP value. The transconductance changes sign slightly above pinch-off at $V \simeq 1.4V_g$, corresponding to a current $I \simeq 1.1I_{sat}$.

II. OVERVIEW OF BALLISTIC PINCH-OFF IN SAMPLE GRS1

A complete panorama of ballistic pinch-off in graphene transistors can be found in sample GrS1, of dimensions $L \times W \times t_{hBN} = 13 \times 17 \times 0.025$ μm, shown in Fig.SI-2. Thanks

to fortuitous equal electron and hole mobilities ($\mu = 6.3$ m^{2}V^{-1}s^{-1}), the current-voltage characteristics in Fig.SI-2-left are fully symmetric. We can distinguish between two different regimes. When $\text{Sign}(V \times V_g) < 0$, increasing V causes an accumulation of charge carriers on the drain side, but the channel stays unipolar. In this case we observe pinch-off-free transport, which shows standard intra-band velocity saturation by optical phonons followed by the Zener inter-band regime with a doping-independent conductance $G_Z(V) \sim 2.5$mS [11]. When $\text{Sign}(V \times V_g) > 0$, pinch-off is observed under drain depletion for a voltage $V \sim V_g$, with broad current saturation plateaus ($V \sim 0.3$–$1.5V_g$). These plateaus terminate as an instability towards the ohmic Zener regime, where charge transport becomes bipolar in the channel. Due to the carrier depletion at the drain, the pinch-off current is depleted below the massless charge neutrality Zener level, suggesting the existence of a doping-induced conductance gap.

The two different transport regimes can also be identified in the transconductance G_m in Fig.SI-2-right. For sake of visibility, we focus here on the $V_g > 0$ curves. The drain carrier accumulation for $V < 0$ is associated with a negative transconductance, as higher gate values, corresponding to higher doping, lead to higher current. On the other hand, the negative values of G_m for positive bias confirm the pinch-off depletion of the current.

Unfortunately, the sample GrS1 suffers from a relatively low electronic mobility and a low dielectric thickness t_{hBN}, which results in a early onset of the Zener conductance and a reduced accessible voltage range. The hBN thickness indeed determines the range of accessible bias and gate voltages that can be applied on the device without generating strong leak currents and finally the breakdown of the insulator [12] ; the leakage can be due to a high gate voltage, but can also appear below the drain electrode if the voltage difference $V - V_g$ becomes too important. As a consequence, the raw differential conductance shows no signature of Schwinger effect.

However, the subtraction of the fitted Klein conductance allows restoring the visibility of the 1d-Schwinger conductance below the Zener onset voltage, as shown in Figure SI-7-a. Further study of this device can be found in Section IV.
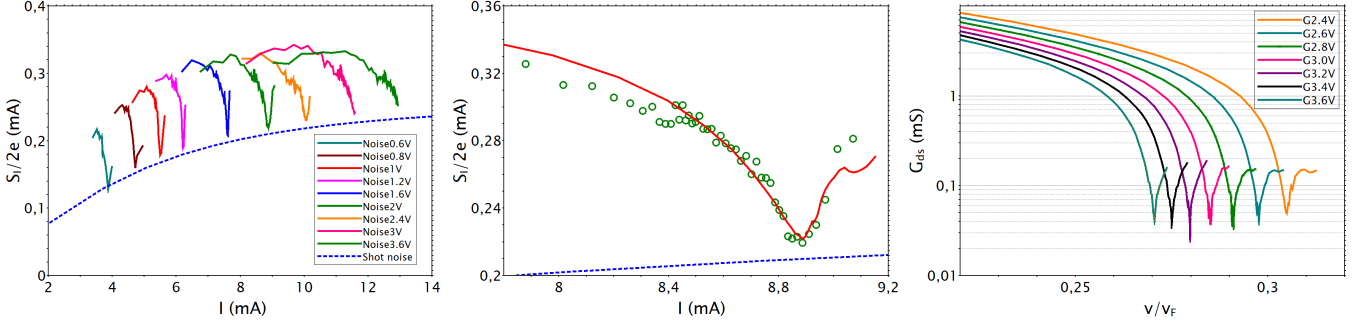
FIG. SI-3: Current noise signature of Klein-collimation pinch-off in sample GrS2. Dimensions are $L \times W \times t_{hBN} = 10.5 \times 15 \times 0.035 \ \mu m$. Left: high-frequency white noise $S_I(I)$, measured at $T_0 = 10$ K in the 1–10 GHz band using Caltech Low Noise Amplifiers (model CITCRYO1-12D). It shows a sharp dip at pinch-off mapping the conductance dip (right panel). Note that the noise dip occurs at a current 10 percent larger than the conductance dip, due to the transconductance correction to the Johnson-Nyquist formula for a transistor $S_{therm} \simeq 4|G + \beta G_m|k_B T_e$. Considering that noise is the sum of a thermal contribution, $S_{th} = 4Gk_B T_e$, and a shot-noise contribution, $S_{shot} = 2eI\mathcal{F}$ where $\mathcal{F} \lesssim 1$ is a Fano factor, we extract the pinch-off shot noise $S_{shot}/2e(I_{sat}) \simeq I_0 \times I_{sat}/\sqrt{I_1^2 + I_{sat}^2}$ (dashed blue line), with $I_0 = 0.26$ mA and $I_1 = 6$ mA. This translates into a tiny pinch-off current Fano factor, $\mathcal{F} = I_{shot}/I_{sat} \simeq I_0/\sqrt{I_{sat}^2 + I_1^2} \lesssim 0.04$, that vanishes for $I_{sat} \gg I_1$. Center: Zoom on the high-frequency white noise $S_I(I)$ close to pinch-off for $V_g = 2V$. Using the measured $G(I)$, we fit noise data (red line) to estimate the electronic temperature on the current saturation plateau ($I \simeq I_{sat}$) at $T_e \sim 1100K \times V/V_g$ ($V_g = 2$ V), which corresponds to $k_B T_e/eV_g \simeq 0.1$. Right: Conductance-velocity $G(v/v_F)$ representation of ballistic pinch-off at $T_0 = 10$ K. The velocity is defined as the velocity at the source electrode by $v = \frac{I}{C_g V_g W}$. In this representation, the broad $V \simeq 1-2V_g$ conductance gap collapses into a singular point at $G(I_{sat}) \lesssim 0.1$ mS.

III.   NOISE CHARACTERIZATION OF KLEIN COLLIMATION

Additional signatures of ballistic pinch-off can be found in the current noise S_I, which is measured in sample GrS2. It is representative of the series and actually quite similar to sample GrS3 of the main text. We distinguish different noise contributions according to frequency: the low-frequency flicker noise, which is measured at sub-MHz frequency and is described in the main text, and the flicker-free white thermal/shot noise, which is measured at GHz frequency.

6

The GHz noise (measured at $T = 10$ K) is plotted in Fig.SI-3-left as function of current. It exhibits a sharp dip at current saturation ($I \gtrsim I_{sat}$) which is reminiscent of the conductance dip observed in the $G(v/v_F)$ data of Fig.SI-3-right. We thus analyze the $S_I(I)$ dependence as the sum of two terms: a thermal contribution $S_{therm} \simeq 4G_{ds}k_BT_e$, where T_e is the hot-electron temperature, and a shot-noise contribution $S_{shot} = 2eI\mathcal{F}$, where $\mathcal{F} \lesssim 1$ is a Fano factor. In this interpretation, the GHz noise dip corresponds to the vanishing of $S_{therm}(I_{sat}) \propto G(I_{sat}) \to 0$ at current saturation, leaving shot noise as the residual noise. This assumption is supported by the $S_I(I) - S_I(I_{sat}) \propto S_{therm}(I)$ dependence which can be fitted in the current saturation regime assuming a $T_e(I) = T_e(I_{sat})V/V_g$ proportional to Joule power $P \simeq I_{sat}V$ (red line in Fig.SI-3-center with $T_e \sim 1100$K for $V_g = 2$ V). Actually, the thermal noise of a transistor, $S_{therm} \simeq 4|G+\beta G_m|k_BT_e$ deviates from the standard Johnson-Nyquist formula for a two terminal resistor by an additive correction proportional to the transconductance G_m. This effect has been demonstrated in carbon nanotube transistors in Ref.[13]. The abrupt sign change of G_m observed at $V/V_g \simeq 1.4$ in Fig.SI-2-right, actually secures a full compensation of the residual conductance which explains the full suppression of thermal noise observed at $I/I_{sat} \simeq 1.1$ in Fig. SI-3-left.

Assigning the $S_I(I_{ds})$ minima to shot noise we deduce a pinch-off shot noise $S_{shot}(I_{sat}) \simeq 2eI_0 \times I_{sat}/\sqrt{I_1^2 + I_{sat}^2}$ (dashed blue line), with $I_0 = 0.26$ mA and $I_1 = 6$ mA. It translates into a tiny Fano factor, $\mathcal{F} = I_{shot}/I_{sat} \simeq I_0/\sqrt{I_{sat}^2 + I_1^2} \lesssim 0.04$, that vanishes for $I_{sat} \gg I_1$. We regard the presence of shot noise as a proof of the existence of a pinch-off junction, and attribute its tiny Fano factor to a consequence of strong collimation effect.

IV. KLEIN-SCHWINGER EFFECT IN THE FULL DEVICE SERIES

Besides the sample GrS3 extensively described in the main text, five other samples have been measured and characterized. All of them show consistent Klein-Schwinger effect, albeit with a somewhat lower visibility due to non-optimal geometrical properties or electronic mobility. Yet, the subtraction of the fitted Klein conductance, following the same procedure as in the main text, allows restoring a larger visibility of the 1d-Schwinger conductance for all the devices. A summary of the properties of the five devices can be found in Table SI-1. For completeness we have reproduced the data of sample GrS3 analyzed in main text.

The current-voltage curves of the six devices series are shown in Figure SI-4. We always

Sample	L	W	t_{hBN}	t_{Graph}	μ	R_c	A	σ_Z	$\frac{V_Z}{V_g}$	$\frac{eV_{sat}}{\mu_s}$	$\frac{V_S}{V_g}$	G_0
	μm	μm	nm	nm	$\frac{m^2}{Vs}$	Ω	-	mS	-	-	-	mS
GrS1	13	17	25	15	6.3	80	50	2.5	1.25	2.6	$0.4 + 0.37\,n_s$	0.17 ± 0.02
GrS2	10.5	15	35	7	13	80	40	1	1.7	3.3	$0.7 + 0.30\,n_s$	0.18 ± 0.01
GrS3	15	10	42	7	12	120	70	1	1.9	2.8	$0.7 + 0.53\,n_s$	0.18 ± 0.02
AuS1	10	13.4	34	/	8	80	7	1.5	1.7	3.7	$0.4 + 0.17\,n_s$	0.18 ± 0.02
AuS2	16	10.6	32	/	13	80	11	1	1.5	4.9	$0.4 + 0.18\,n_s$	0.18 ± 0.01
AuS3	11.1	11.4	90	/	11	95	100	0.7	1.6	/	$0.7 + 1.05\,n_s$	0.17 ± 0.04

TABLE SI-1: Summary of the properties of the device series studied in the main text (GrS3) and in the supplementary (GrS1 and GrS2, AuS1, AuS2, AuS3). Base parameters presented in the first columns include the geometrical properties L, W, t_{hBN}, t_{Graph} for the devices on graphite gate, mobility and contact resistance. Also displayed is the maximum value of the voltage gain $A = \frac{\partial V}{\partial V_g}$. The next 4 columns correspond to the parameters that are responsible for the unveiling and visibility of the Klein-Schwinger effect in the different devices : V_Z is the Zener onset voltage, where a Zener conductance σ_Z activates. It has to be (notably) higher than the Schwinger voltage V_S that triggers the Schwinger conductance, and whose doping dependence is shown in the next-to-last column. The doping-dependent saturation voltage V_{sat}, extracted from the dependence $G = G(0)Exp\left[-\frac{V}{V_{sat}}\right]$ in the Klein regime, is a metrics of the Klein collimation and defines the beginning of the conductance gap, later terminated by Zener regime. The last column G_0 corresponds to the zero-bias affine extrapolate of the Schwinger pair conductance, as explained in the main text.

subtract in the bias voltage the voltage drop $R_C I$ across the contact resistance. All the devices exhibit broad current saturation plateaus, with, however, an incomplete saturation (differential resistance peak $G^{-1} \lesssim 5k\Omega$) for devices AuS1 (panel d) and Au-S2 (panel e). The current saturation plateaus are terminated by the onset of Zener conductance at a Zener field $V_Z = 1.25 - 2V_g$ depending on the device. Detailed values can be found in Table SI-1.

All six devices exhibit consistent Klein collimation, as is described by the semi-log representation of the differential conductance scaling $G(V/V_g)$ in Figure SI-5. It shows an exponential decay of the Klein conductance for all samples, with a sample-dependent slope that tunes the depth of the conductance gap. For instance, sample AuS3 (panel f) exhibits a
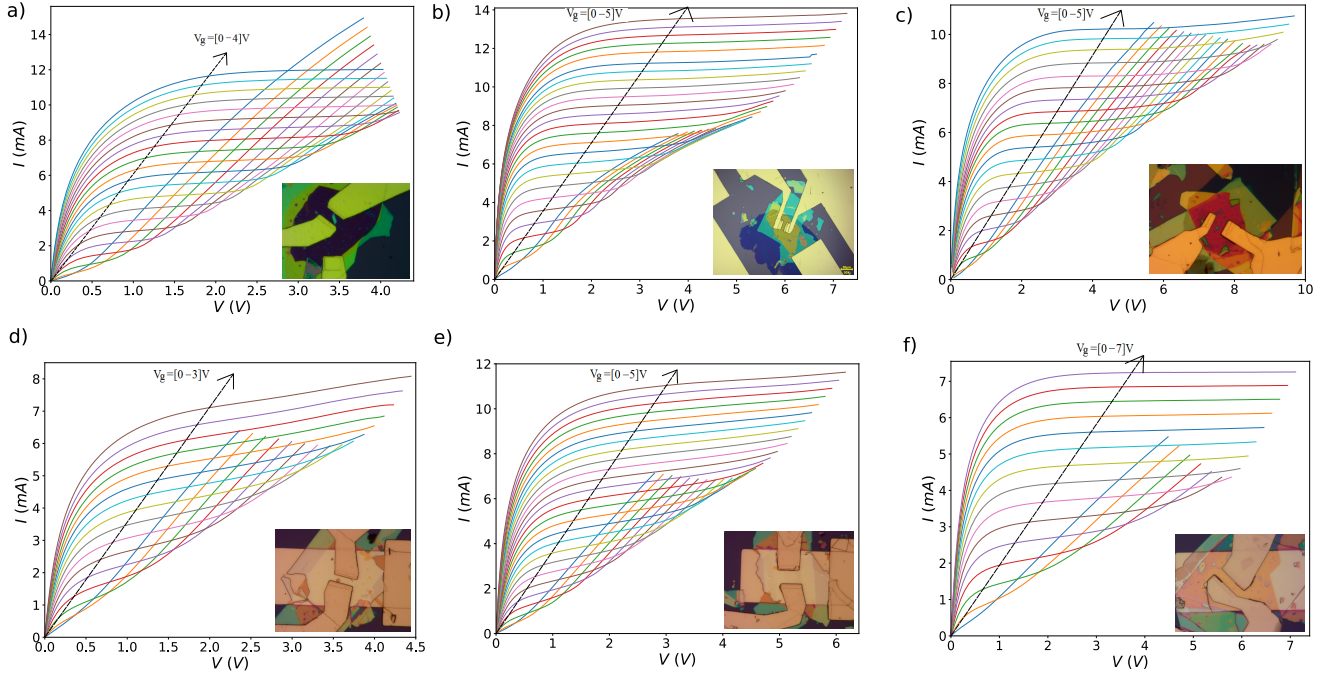
FIG. SI-4: Current-voltage curves of the device series GrS1 (panel a), GrS2 (panel b), GrS3 (panel c), AuS1 (panel d), AuS2 (panel e) and AuS3 (panel f). Inset of each panel shows an optical image of the device. Actual device dimensions and properties for the series are collected in Table SI-1. The applied gate voltages correspond to a charge carrier density at the source ranging from 0 to $1.5 - 2.5 \ 10^{12} \, \mathrm{cm}^{-2}$ depending on the device.

steep conductance decay by three orders of magnitude at pinch-off, with differential conductance dropping below 10μS, whereas the conductance gap is very shallow in samples AuS1 (panel d) and AuS2 (panel e). The doping-dependent saturation voltage V_{sat}, plotted in inset in the different panels, presents consistently a linear relation with the doping $eV_{sat} = \alpha\mu_S$ with $\alpha \sim 3$ in the different samples (except for AuS3 where $V_{sat} = Cte$, see Table SI-1).

In order to study 1d-Schwinger pair conductance in the full series, Figure SI-6 shows a zoom of the differential conductance as function of V/V_g in the conductance gap region, where Schwinger conductance appears on top of current saturation. The visibility of Schwinger effect differs on the different devices, yet the 3-parameters KSE fits closely match the data on all of them (dotted lines in the figure). Sample GrS1 (panel a) demonstrates a very narrow conductance gap due to early Zener onset at $V_Z \sim 1.25V_g$, hiding Schwinger conductance. Samples GrS2 and GrS3 (panel b and c) are very similar and both exhibit a wide conductance gap due to a complete current saturation and a rejection of the Zener voltage above $1.7V_g$.
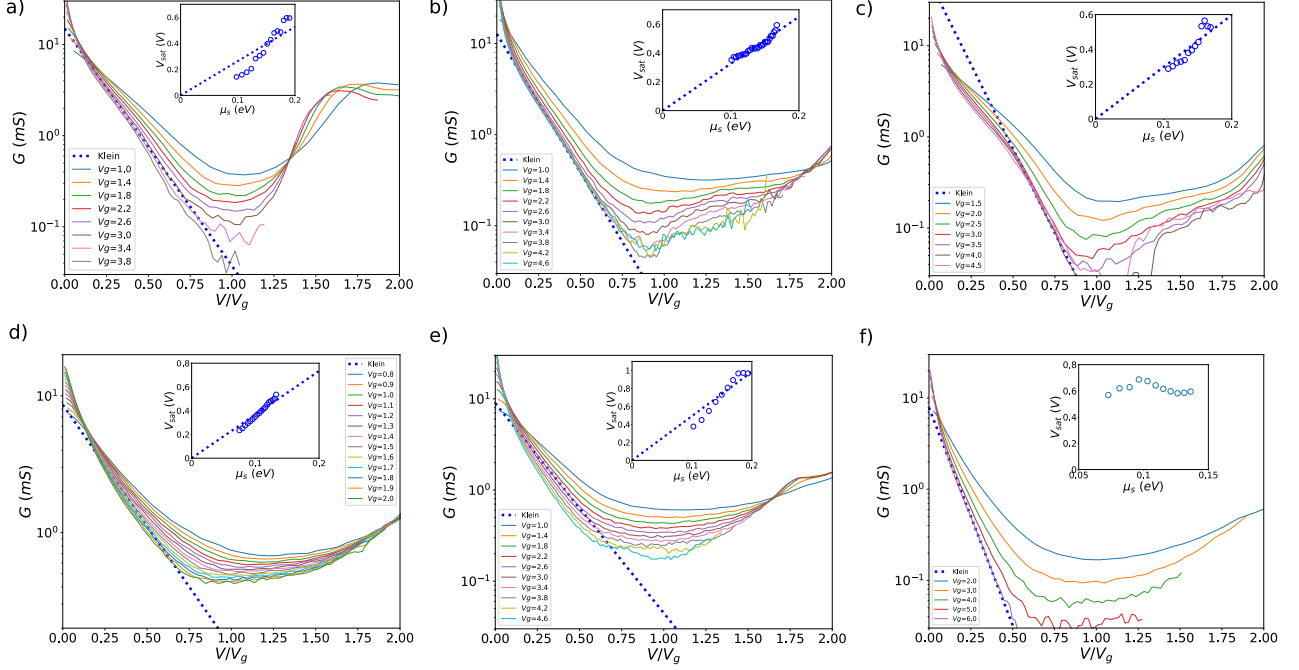
FIG. SI-5: Semi-log representation of the differential conductance scaling $G(V/V_g)$, showing the exponential decay of the saturation dependence $G = G(0)exp(-\frac{V}{V_{sat}})$ (dotted blue line) for the device series GrS1 (panel a), GrS2 (panel b), GrS3 (panel c), AuS1 (panel d), AuS2 (panel e) and AuS3 (panel f). Inset of each panel shows the evolution of the saturation voltage V_{sat} as function of the doping, with a linear relation for all devices except AuS3. Numerical values can be found in Table SI-1.

Due to the Klein conductance $G_K \propto W$ and the Zener threshold set by Pauli blocking $V_Z \propto L$, sample GrS2 exhibits a narrower conductance gap compared to GrS3. 1d-Schwinger conductance is still clearly visible in the conductance gap.

The devices on Au gates have a lower visibility for the Schwinger conductance here. Sample AuS1 (panel d) and AuS2 (panel e), whose properties are very similar (see Table SI-1), demonstrate a very shallow conductance gap $G_{min} \sim 0.2 - 0.4$mS, making it uneasy to see a direct signature of Schwinger regime via its onset. Sample AuS3 (panel f), with its thicker dielectric $t_{hBN} = 90$nm, exhibits an extremely deep and large conductance gap. However, the large dielectric thickness also shifts the Schwinger voltage towards higher values $V_S \gtrsim 1.5V_g$, setting the onset of the Schwinger conductance near the Zener onset and therefore reducing its visibility.

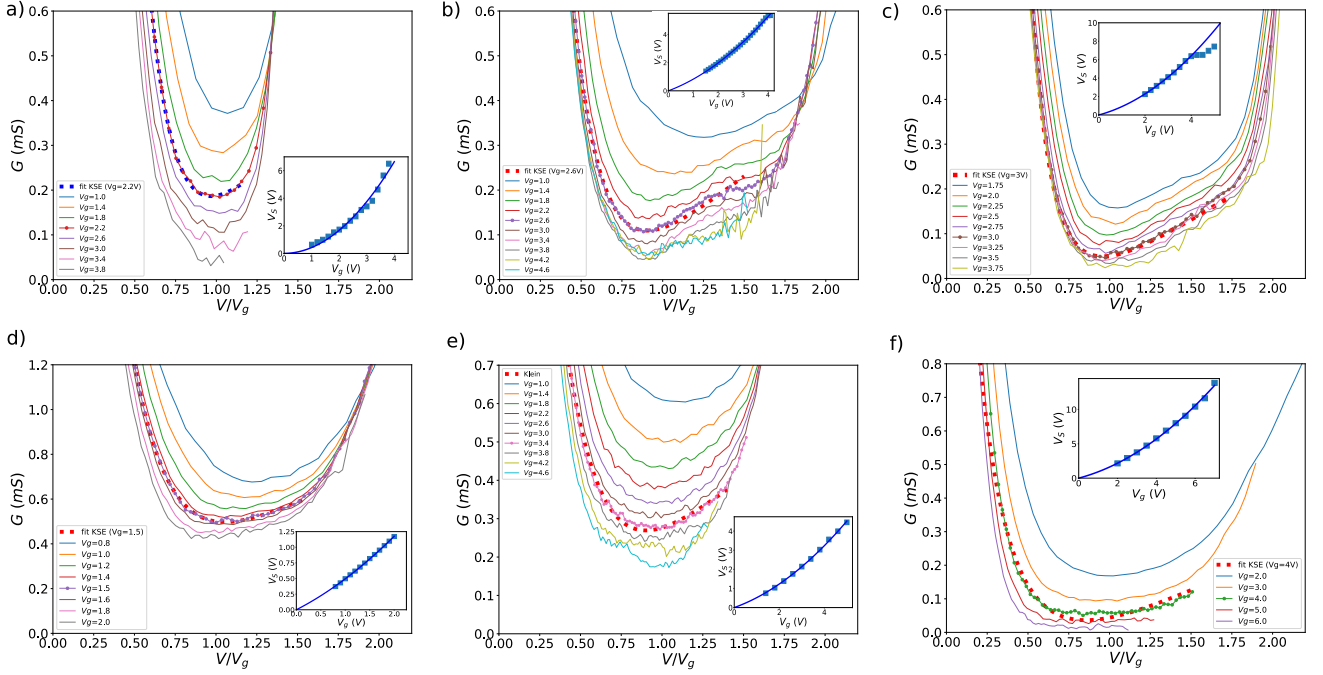The KSE fits performed on the 6 devices give the values of the Schwinger voltage V_S, which

10

FIG. SI-6: Klein-Schwinger effect in the sample series GrS1 (panel a), GrS2 (panel b), GrS3 (panel c), AuS1 (panel d), AuS2 (panel e) and AuS3 (panel f). The red dotted lines on each figure show an example of a three-parameter fit $G = G_S(V_S) + G(0)e^{-V/V_{sat}}$ performed in the $V_{sat} \lesssim V \lesssim V_Z$ range ; due to different geometrical and electronic properties, the Schwinger visibility is variable on the different devices. Inset in each panel shows the super-linear dependence of the Schwinger voltage as function of gate voltage $\frac{V_S}{V_g} = a + bn_s$ deduced from the fits. The values of the coefficients a and b can be found in Table SI-1 for each device.

is plotted in the insets as function of the gate voltage V_g. For analysis of these data, we refer to Figure 3-c in the main text.

The visibility of the 1d-Schwinger pair conductance is determined by the combined vanishing of Klein intraband conductance and Zener interband conductance. Using the KSE fits, performed in Klein and Schwinger regimes, the subtraction of the fitted contribution of Klein conductance allows revealing the Schwinger conductance on a broader range of bias, a procedure which has been described in the main text (see Figure 3-b). The resulting pair conductance $G_S(V)$ is plotted for all devices in Figure SI-7, revealing ubiquitous 1d-Schwinger conductance for the sample series. Agreement with the theoretical formula (solid lines) is excellent, up to a a Zener voltage corresponding to a steep increase of pair conductance.
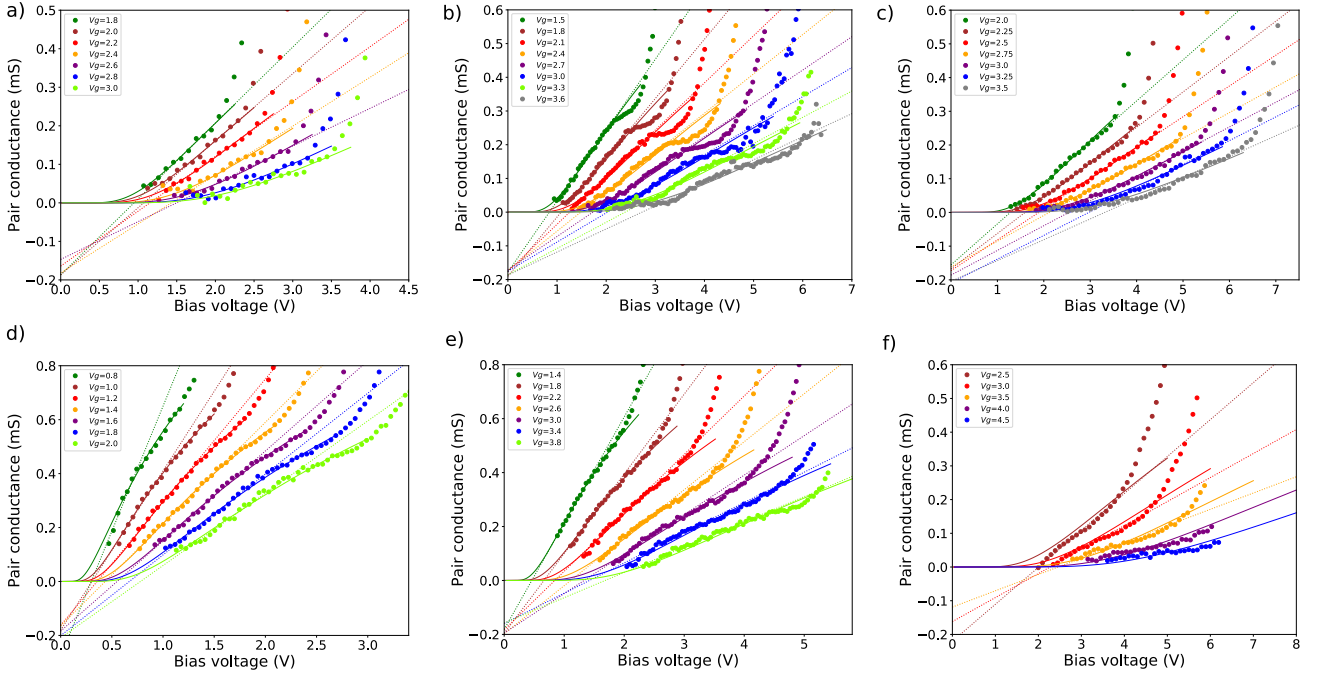
FIG. SI-7: Pair conductance of the device series GrS1 (panel a), GrS2 (panel b), GrS3 (panel c), AuS1 (panel d), AuS2 (panel e) and AuS3 (panel f), obtained from data by subtracting the fitted Klein conductance. Pair conductance can be fitted using the 1d-Schwinger formula (solid lines) over a device-dependent range of bias, highlighting the presence of Schwinger conductance in all devices. The 'affine approximation' extrapolates at zero bias (dotted lines) collapse onto one universal value $G_0 \simeq 0.18$ mS which appears doping- and device-independent. Exact values of the extrapolate can be found in Table SI-1.

Whereas the 1d-Schwinger conductance was already clearly visible in samples GrS2 and GrS3 (panels b and c), the subtraction reveals large Schwinger conductance in sample AuS1 and AuS2 (panels d and e) that was previously obscured by Klein conductance exponential decay. Due to the low value of the Schwinger voltage $V_S \sim 0.5 - 0.7 V_g$ in these last two devices, Schwinger pair conductance is visible on a wider bias range before Zener conduction sets in, unveiling the non-linearity of Schwinger conductance at high bias voltages which is discussed in the main text (Fig.3-d).

The universality of 1d-Schwinger conductance is revealed by the zero-bias 'affine approximation' extrapolate, that gives a unique value $G_0 \simeq 0.18$mS for all gate voltages and for each of the 6 devices of the series, despite a broad variation of geometrical parameters and electronic mobility. This value closely follows the theoretical expectation $G_0 = 0.186$mS

from Schwinger formula.

Unveiling the visibility of Klein-Schwinger effect is thus an optimization task of the different geometrical parameters; the five devices in this Supplementary Information Section were in fact used to set the optimal visibility properties of the sample GrS3, which is used as a demonstrator in the main text. Prerequisites are a low contact resistance and a very high electronic mobility $\mu \gtrsim 10\mathrm{m}^2\mathrm{V}^{-1}\mathrm{s}^{-1}$. The hBN optimal thickness is a trade-off: thin layers cause dielectric breakdown problems and confine V_S below pinch-off, generating an early Schwinger conductance onset that can only be revealed by subtraction. Thick layers shift the Schwinger voltage upwards, eventually above the Zener onset terminating the conductance gap. Klein-Schwinger effect is more easily visible in long channel transistors, due to the Pauli-blocked Zener voltage, and devices with a smaller width favor the Klein-collimation and the appearance of 1d-Schwinger effect.

V. RELATION BETWEEN SCHWINGER VOLTAGE, DOPING AND DIELECTRIC THICKNESS

The variety of devices studied in Section IV allows us to analyze the dependencies between Schwinger voltage, doping and dielectric thickness. Figure 3-c of the main text, and the forelast column of Table SI-1, show the evolution of the ratio between Schwinger voltage and gate voltage V_S/V_g as function of doping n_s for the 6 devices. They consistently show a linear increase with respect to n_s that we can attribute to a Coulomb-repulsion effect from the interactions, with a slope that is device-dependent. This slope is plotted as function of the thickness of the hBN dielectric in Figure SI-8. For the case of devices on graphite backgates, the hBN thickness has been replaced by the sum of t_{hBN} and the graphite thickness t_{Graph}, whose values are given in Table SI-1. This relies on the existence of a Debye length for neutral graphite that we approximate to be the total thickness of the thin graphite flake. The slope exhibits an affine increase as function of hBN thickness, and extrapolates to zero for $t_{hBN} \sim 20$nm. This value is on the order of the Fermi wavelength for typical doping range $n_s = 1 - 2 \; 10^{12}\mathrm{cm}^{-2}$, which acts as a cut-off for interaction effects.

Let us make the assumption that the Schwinger gap $\Delta_S \sim \mu_s$ which is the only energy scale of the problem. Then, the dielectric thickness t_{hBN} being the only lengthscale of the problem, the doping dependence of the junction length $\Lambda(n_s, t_{hBN})$ can be cast in the form

$\frac{\Lambda}{t_{hBN}} = \frac{V_S/E_S}{V_g/E_g} = 4\alpha_g(\frac{\mu_s}{\Delta_S})^2\frac{V_S}{V_g} \simeq 2.8\frac{V_S}{V_g}$ where $\alpha_g = \frac{e^2}{4\pi\epsilon_0\epsilon_{hBN}\hbar v_F} = 0.70$ is the graphene fine structure constant, taking the high-field hBN permittivity $\epsilon_{hBN} \simeq 3.1$ [12].

The measured evolution of $\frac{V_S}{V_g}(t_{hBN}, n_s)$ described in Figure 3-c of the main text and Figure SI-8 can thus be cast into the junction length power expansion $\Lambda \simeq a t_{hBN} + \xi n_s t_{hBN}^2$. Numerical values of Λ are indicated on the right axis in Figure SI-8 and yield $\xi \simeq 4$nm, which corresponds to the typical interaction radius per electron , quantifying the doping-induced dilation of the junction length.
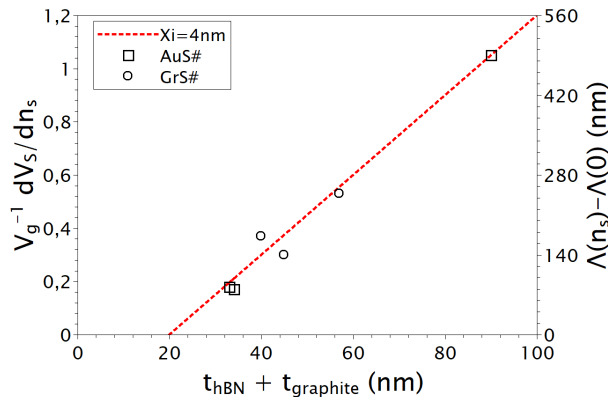

FIG. SI-8: Slope extracted from the linear increase of the ratio $\frac{V_S}{V_g}$ as function of doping n_s (left axis), plotted with respect to the sum of hBN and graphite thicknesses for the 6 devices. Right axis gives the associated value of the junction length $\Lambda(n_s)$. The red dotted line is a linear fit corresponding to $\xi = 4$nm.

The direct consequence of these dependencies is that the 1d-Schwinger conductance becomes hardly visible for devices with thick dielectric such as AuS3, where the Schwinger voltage exceeds the Zener onset voltage even at moderate doping. On the contrary, devices with thin dielectric show an early Schwinger conductance over a large range of doping.

VI. PINCH-OFF OF HIGH-MOBILITY GRAPHENE TRANSISTORS

We first start with a comparison between pinchoff and pinchoff-free characteristics. As a general rule, finite biases induce both doping and voltage drops in transistors, which are proportional to the source-drain voltage. The difference between pinchoff and pinchoff-free cases is about their spatial distributions: in the pinchoff case, they are confined at the drain side, whereas in the pinchoff-free case they are distributed along the channel. In the pinchoff-
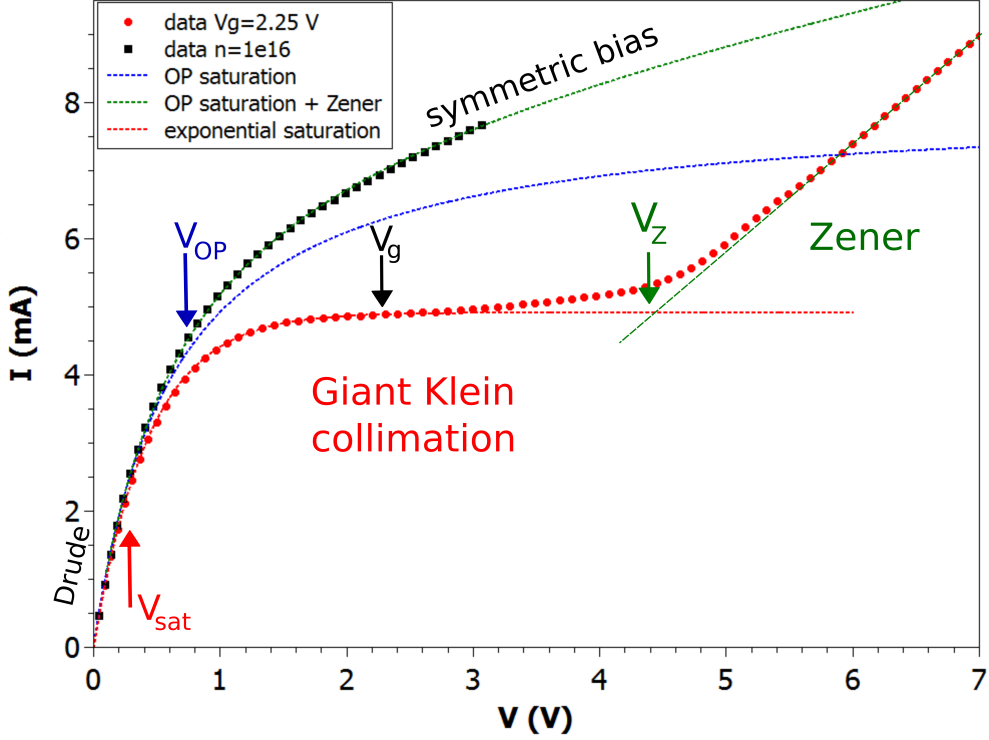
FIG. SI-9: Comparison between pinchoff and pinchoff-free regimes in sample GrS3 at the carrier density $n_s = 10^{12}$ cm^{-2}. Black dots correspond to measurements at fixed $V_g = 2.25$V, whereas red squares correspond to a measurement along constant density line $V_g(V) = V_g + 0.4V$ with V the bias voltage, for the same density. The current saturation in the pinch-off free case can be fitted using saturation by optical phonons (blue dotted line, with the green dotted line adding the contribution of interband Zener conductance) with $\epsilon_{sat} = 91$ meV, showing that the bottleneck of current saturation at constant V_g is not due to optical phonons but to the pinch-off. Red dotted line is a fit for an exponential current saturation at pinch-off.

free diffusive regime of bottom/top gated transistors, the bias voltage entails a uniform doping gradient along the channel from $n_s = C_g(V_g)/e$ at the source to $n_d = C_g(V_g - V)/e$ at the drain. The pinchoff-free regime is achieved by applying a bias-dependent gate voltage $V_g(V) = V_g(0) + aV$ with $a \sim 0.5$ mimicking a symmetric $\pm V/2$ bias. Experimentally $a \simeq 0.4$ is adjusted to obtain a bias-independent charge neutrality point position. In the pinchoff case, most of the doping gradient is localized at the drain in a pinchoff junction, leaving the doping quasi uniform in the channel.

Fig.SI-9 shows the contrasted pinchoff (red circles) and pinchoff-free (black circles) char-

acteristics of sample GrS3, for a carrier density $n_s = 10^{12}$ cm^{-2}. Both deviate at V_{sat}, with the pinchoff I-V (asymmetric bias) showing an exponential current saturation (red dotted line), as opposed to the pinchoff-free (symmetric bias) I-V which shows strong non-linearities but does not saturate. These non-linearity is qualitatively understood (green dotted line) in terms of optical-phonon-induced velocity saturation (blue dotted line) with a characteristic voltage V_{OP} , and interband Zener tunneling as captured by the formula

$$I = n_s e \left[\frac{\mu}{1 + V/V_{OP}} + \sigma_Z \right] \frac{W}{L} V \quad , \tag{8}$$

with $\mu \simeq 12$ m^2/Vs, $V_{OP} \simeq 0.65$ V $> V_{sat}$, and $\sigma_Z \simeq 0.5$ mS. In the following we go beyond that phenomenological description by solving a simple 1d-model of the electrostatic potential distribution in the channel.
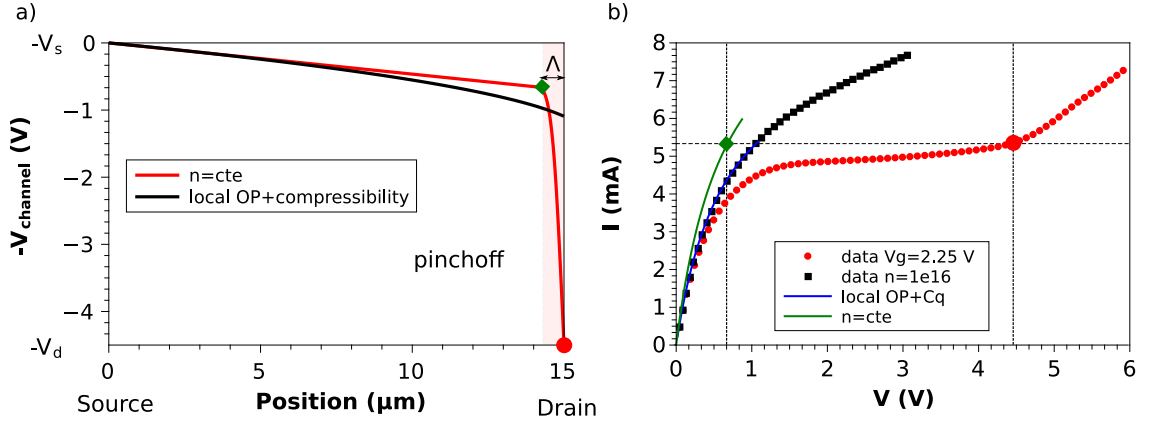

FIG. SI-10: Panel a) Electrostatic profile in the constant density case and in the pinchoff-free case, with an excess potential drop at the drain. Both profiles are computed for a 5.4mA current. Panel b) Current-voltage curves in the two biasing regimes. The green black line corresponds to the constant density model of the channel described in the text, and the blue-line fit is performed with the microscopic model presented in the text. The horizontal dashed line corresponds to the 5.4mA current of panel a. The geometrical construction allowing to recover the potential drop in the channel and at pinchoff is indicated on the figure by the bold symbols.

Focusing on the pinchoff-free case, we estimate the electrostatic potential profile by solving a local microscopic model of transport including: velocity saturation by OPs, electronic compressibility, and electrostatic equilibrium in the presence of a local gate. Dealing with

16

current lass than or on the order of pinchoff saturation currents, we neglect the Zener tunneling contribution (see Fig.SI-9).

The current density writes

$$J = \mu(E) n \partial_x \mu_c^*,$$

where $\mu(E) = \mu(0)/(1 + |E|/E_{OP})$ is the electric-field-dependent mobility accounting for OP velocity saturation in Eq.(8), $\mu(0)$ is the zero-bias mobility, $\mu_c^* = \mu_c(x) - eV_c(x)$ and $\mu_c(x)$ the electrochemical and chemical potentials. V_c is the electrostatic potential distribution of interest in this section. For monolayer graphene, $\mu_c^* - \mu_g^* = \hbar v_F \sqrt{\pi n} + \frac{e^2}{c_g} n$ where v_F is the Fermi velocity, c_{geo} is the areal gate-channel geometric capacitance, $n(x)$ is the carrier density, and $\mu_g^* = -eV_g$ is the uniform electrochemical potential of the gate. Additionally, electrostatics imposes $V_c - V_g = \frac{-e}{c_{geo}} n(x)$, so that the differential equation for the channel voltage writes :

$$J = \frac{I}{W} = -\frac{\mu_0}{1 + |\partial_x V_c|/E_{OP}} c_{geo}(V_c - V_g) \left\{ \frac{\hbar v_F}{e} \sqrt{\frac{\pi c_{geo}}{e}} \frac{1}{2\sqrt{V_g - V_c}} + 1 \right\} \partial_x V_c \quad , \quad (9)$$

where $E_{OP} = V_{OP}/L$ is the OP saturation electric field.

We numerically solve this equation for currents in the range $[0-5]$mA imposing $V_d + V_s = 0$, and $V_g = -2.25$ V to match the experimental conditions and find perfect agreement (solid blue line in Figure SI-10b) with the IV experimental response for $\mu(0) = 12.3$ m^2.V^{-1}.s^{-1}, $E_{OP} = 43$ mV/μm. Using this set of parameters, we next compute the channel potential profile at the current saturation in the pinchoff-free case for a 5mA current, which is plotted as a black line in Figure SI-10a. The total channel voltage drop, $V_c(L) = 1$ V (see large black dot in Fig.SI-SI-10b).

To model the pinchoff case, we assume a constant carrier density in the channel, which implies a constant chemical potential and uniform in-plane electric field. As a consequence, the differential equation (9) simplifies as :

$$J = -\frac{\mu_0}{1 + |\partial_x V_c|/E_{OP}} n \ \partial_x V_c$$

.

The electrostatic energy profile in this case for a 5.4mA current is plotted in Fig. SI-10a (red line) up to the drain-collimation junction where potential is assumed to drop abruptly down to the applied voltage $V = 4.5$ V. The total channel voltage drop, $V_c(L - \Lambda) \simeq 0.5$ V remains small with respect to the total bias 4.5 V, ass assumed in the main text.

17

Fig. SI-10b summarizes the conclusions of our potential distribution analysis. At a given bias current, the respective channel and junction potential drops can be deduced by the geometrical construction displayed in the figure.

[1] C. Itzykson and J.B. Zuber, *Quantum Field Theory*, Dover publications, 2006.

[2] S.M. Sze and K. Ng, *Physics of Semiconductor Devices, Wiley-2007-3rd edition*, Section X.X.X.

[3] M.A. Grado-Caffaro, M. Grado-Caffaro, *Optik* **116**, 299 (2005). *Electrical conductance from the Fowler-Nordheim tunneling*

[4] S.P. Gavrilov. and D.M. Gitman, *Phys. Rev. D* **53**, 7162 (1996). *Vacuum instability in external fields*

[5] A. Shytov, M. Rudnerb, N. Guc, M. Katsnelson, L. Levitov, *Solid State Communications* **149**, 10987 (2009). *Atomic collapse, Lorentz boosts, Klein scattering, and other quantum-relativistic phenomena in graphene*

[6] B. Dora, R. Moessner, *Phys. Rev. B* **81**, 165431 (2010). *Non-linear electric transport in graphene: quantum quench dynamics and the Schwinger mechanism*

[7] S. P. Gavrilov, D. M. Gitman, N. Yokomizo, *Phys. Rev. D* **86**, 125022 (2012). *Dirac fermions in strong electric field and quantum transport in graphene*

[8] N. Vandecasteele, A. Barreiro, M. Lazzeri, A. Bachtold, F. Mauri, *Phys. Rev. B.* **82**, 045416 (2010). *Current-voltage characteristics of graphene devices: Interplay between Zener-Klein tunneling and defects.*

[9] J. Tworzydlo, B. Trauzettel, M. *Phys. Rev. Lett.* **96**, 246802 (2006). *Sub-Poissonian shot noise in graphene*

[10] R. Danneau, F. Wu, M. F. Craciun, S. Russo, M. Y. Tomi, J. Salmilehto, A. F. Morpurgo, P. J. Hakonen, *Phys. Rev. Lett.* **100**, 196802 (2008). *Shot Noise in Ballistic Graphene*

[11] W. Yang, S. Berthou, X. Lu, Q. Wilmart, A. Denis, M. Rosticher, T. Taniguchi, K. Watanabe, G. Fève, J.M. Berroir, G. Zhang, C. Voisin, E. Baudin, B. Plaçais, *Nature Nanotechnol.* **13**, 47 (2018). *A graphene Zener-Klein transistor cooled by a hyperbolic substrate*

[12] A. Pierret, D. Mele, H. Graef, J. Palomo, T. Taniguchi, K. Watanabe, Y. Li, B. Toury, C. Journet, P. Steyer, V. Garnier, A. Loiseau, J-M. Berroir, E. Bocquillon, G. Fève, C. Voisin, E. Baudin, M. Rosticher, B. Plaçais, *Materials Research Express* in press https://doi.org/10.1088/2053-1591/ac4fe1 (2022). *Dielectric permittivity, conductivity and breakdown field of hexagonal boron nitride*

[13] J. Chaste, E. Pallecchi, P. Morfin, G.Fève, T. Kontos, J.-M. Berroir, P. Hakonen, B. Plaçais,

Appl. Phys. Lett. **96**, 192103 (2010) *Thermal shot noise in top-gated single carbon nanotube field effect transistors*

[14] I. Meric, M. Y. Han, A. F. Young, B. Ozyilmaz, P. Kim, K. L. Shepard, *Nature Nanotech.* **3**, 654-659, (2008). *Current saturation in zero-bandgap, top-gated graphene field-effect transistors*

[15] Q. Wilmart, M. Boukhicha, H. Graef, D. Mele, J. Palomo, M. Rosticher, T. Taniguchi, K. Watanabe, V. Bouchiat, E. Baudin, J-M. Berroir, E. Bocquillon, G. Fève, E. Pallecchi, B. Plaçais, *Appl. Sci.* **10**, 446, (2020). *High-Frequency Limits of Graphene Field-Effect Transistors with Velocity Saturation*